

VLBI IMAGING OF THE 86 GHz SiO MASER EMISSION IN THE CIRCUMSTELLAR ENVELOPE OF VX SAGITTARII

SHEPERD S. DOELEMAN AND COLIN J. LONSDALE

MIT Haystack Observatory, Off Route 40, Westford, MA 01886¹; dole@newton.haystack.edu, cjl@newton.haystack.edu

AND

LINCOLN J. GREENHILL

Harvard-Smithsonian Center for Astrophysics, 60 Garden Street, Cambridge, MA 02138; greenhill@cfa.harvard.edu

Received 1997 June 9; accepted 1997 September 17

ABSTRACT

We have observed and imaged the SiO maser source in the late-type star VX Sgr with a single VLBI baseline at 3.5 mm wavelength. Phase-referenced channel maps with a beamwidth of ~ 0.4 mas show multiple components over a LSR velocity range of -1 to 24 km s⁻¹, and many of the maser features display velocity widths smaller than 1 km s⁻¹. The maser spots in this 86 GHz transition ($v = 1$, $J = 2 \rightarrow 1$) are arranged in an irregular ring-shaped configuration of diameter ~ 30 mas, echoing the structures found in the $J = 1 \rightarrow 0$ transition at 43 GHz around several Mira variables and VX Sgr itself. Unlike previous observations of SiO masers, in VX Sgr we detect a clear, systematic velocity gradient of ~ 0.6 km s⁻¹ AU⁻¹ among the strongest complex of masers on the southernmost portion of the ring structure. This velocity gradient can be interpreted as a rigid rotation of the circumstellar envelope with $v \sin i \sim 13$ km s⁻¹. Maser emission is not detected on long (5000 km) baselines, which places a 0.1 mas lower limit on the size of strong maser spots.

Subject headings: masers — circumstellar matter — radio lines: stars — stars: individual (VX Sagittarii)

1. INTRODUCTION

Circumstellar masers are often associated with late-type stars, generally Mira variables and supergiants. Their circumstellar envelopes exhibit strong H₂O and OH maser radiation, and there is compelling evidence that these masers originate in an accelerating dusty mass-loss flow (Chapman & Cohen 1986). However, the SiO masers seem to have different loci. They occur inside the inner radius of the dust shell, very close to the stellar photospheres, possibly in a region of less organized outflow (e.g., Greenhill et al. 1995). VLBI experiments have demonstrated that the masers lie in ringlike configurations, presumably centered on the star, with tangential rather than radial maser gain paths (Diamond et al. 1994; Miyoshi et al. 1994; Greenhill et al. 1995; Humphreys et al. 1996; Kemball & Diamond 1997). The ring radii appear to be of order 2 stellar radii. The masers are variable in structure and intensity, usually echoing the periodic optical light curve with a small delay (Elitzur 1992) and with line-shape variations on timescales as short as 10–20 days (Pijpers, Pardo, & Bujarrabal 1994). The most recent data show systematic variations in ring radius as a function of time (Diamond, Kemball, & Boboltz 1997). Strong linear polarization is observed from these masers (McIntosh & Predmore 1993; Kemball & Diamond 1997), and weaker circular polarization is also observed (Barvainis & Predmore 1985; McIntosh, Predmore, & Patel 1994), suggestive of strong, ordered, and dynamically important magnetic fields close to these stars (Kemball & Diamond 1997; Elitzur 1996; but also see Nedoluha & Watson 1994). The velocity structure of the masers is generally disordered, although weak trends have been noted (Diamond et al. 1994; Greenhill et al. 1995).

The SiO maser pump mechanism remains uncertain, and

analyses of both collisional pumping (Elitzur 1992; Miyoshi et al. 1994; Lockett & Elitzur 1992) and radiative pumping (Rausch et al. 1996; Bujarrabal 1994a, 1994b) can be found in the literature. While both mechanisms appear feasible, collisional pumping may be a simpler and more efficient process for powering these masers, which are often exceedingly strong. VX Sgr, with variable peak line intensities sometimes reaching a few hundred janskys at a presumed distance of 1.7 kpc, is among the most luminous of its class. Radiative pumping models remain plausible, though they require more complex, and in some sense more contrived, circumstances in order to reproduce the observations satisfactorily. A generalized model that permits both collisional and radiative pumping (Doel et al. 1995) produces good fits to the Mira variable variety of SiO masers with primarily collisional pumping at a temperature of 1500 K and densities $n(\text{H}_2) \sim 5 \times 10^9$ cm⁻³.

The maser emission generally occurs most strongly in the $v = 1$, $J = 1 \rightarrow 0$ and $J = 2 \rightarrow 1$ transitions at 43 GHz and 86 GHz, respectively, though emission in other rotational transitions and at higher vibrational states exists. The lack of consensus regarding the pump mechanisms, and consequently the underlying physical conditions within the masing regions, emphasizes the need for observational data capable of constraining the pump mechanism. In general, this means characterization of maser spots from different transitions, if there is more than one, that originate in the same volume of gas. Consequently, efforts have been made to measure the degree of spatial coincidence between 43 GHz and 86 GHz masers. Such efforts, exemplified by the work of Colomer et al. (1996), have necessarily suffered from a lack of spatial resolution at 86 GHz, since the best instruments available to study the stars at this frequency have been connected-element millimeter-wave interferometers with fringe spacings on the order of 1". By comparison, the proximity of the masers to the stellar photosphere dictates a total angular extent of the maser region measured in tens of

¹ Radio astronomy at the Haystack Observatory of the Northeast Radio Observatory Corporation (NEROC) is supported by a grant from the NSF.

milliarcseconds at most. While current data, bolstered in isolated cases by coincidences in line shapes and polarizations in the different transitions (McIntosh & Predmore 1993), support the hypothesis of cospatiality, the tests for spatial separation have not been very sensitive. This is less true for masers from different vibrational states, but the same rotational transition, after the work of Miyoshi et al. (1994), which achieved positional registration at the 2 mas level for $v = 1$ and $v = 2$ 43 GHz ($J = 1 \rightarrow 0$) masers in two stars.

In this paper we describe VLBI observations at 86 GHz of VX Sgr that provide information on the spatial distribution of the 86 GHz masers with submilliarcsecond resolution. VX Sgr is notable among evolved stars whose circumstellar envelopes support SiO masers because it is unusually large with a radius of 22 AU, given an assumed distance of 1.7 kpc (Greenhill et al. 1995, and references therein). Moreover, its mass-loss rate, as estimated by Knapp & Morris (1985), is between 10^{-5} and $10^{-4} M_{\odot} \text{ yr}^{-1}$, at least an order of magnitude larger than that of TX Cam, a Mira variable whose SiO maser emission has recently been mapped (Kemball & Diamond 1997). Indeed, VX Sgr is classified as a red supergiant star, a distinction dependent on its true distance, which is a topic of some debate. Estimates of its distance range from 238 pc (Celis 1995) to 2 kpc (Alter, Balázs, & Ruprecht 1970). We follow Greenhill et al. (1995) and use 1.7 kpc in part to facilitate comparison with their work. The pulsations giving rise to the mass loss and extended envelope of VX Sgr are semiregular with a period of 732 days (Kholopov et al. 1987). We observed VX Sgr at an optical phase of $\phi \sim 0.2$, a phase that historically corresponds to near-peak SiO emission.

The observation reported here provides accurate relative positions of the strongest maser spots at 86 GHz. Although no registration to maser emission at 43 GHz is possible, we are able to demonstrate the feasibility of future simultaneous 43 GHz and 86 GHz VLBI observations of VX Sgr and other stars in order to yield precision relative astrometry between maser spots at the two frequencies, in principle with positional accuracies of a few tens of microarcseconds. Such measurements would represent an exquisitely sensitive test of intravibrational state maser cospatiality, and thereby contribute to our detailed understanding of these sources.

In § 2 we describe the observations and data reduction process, with particular emphasis on (1) the technical problems associated with complex source structure in position and velocity and (2) the atmospheric coherence properties associated with VLBI at high frequencies. In § 3 we deal with the implications of the current results and discuss the prospects for future progress, while in § 4 we present our conclusions.

2. OBSERVATIONS AND DATA REDUCTION

2.1. Observations

We observed VX Sgr over the time range 0930–1615 UT on both 1994 April 2 and 1994 April 4 with an array of three VLBI antennas. During this time, Sgr A*, the compact radio source in the Galactic center, was the prime scientific target, and scans on both VX Sgr and NRAO 530 were included in the program to assist with amplitude calibration (Rogers et al. 1994). The total time allocated to VX Sgr was only one 3 minute scan every 20 minutes. Participating

VLBI stations were the Haystack Observatory, the Kitt Peak radio telescope, and four phased elements of the Owens Valley Radio Observatory (OVRO) array. Characteristics of each telescope and average system equivalent flux densities (SEFD) near 40° elevation are given in Table 1. Pointing was nominal at all sites with accuracy at the 5" level. For baselines to OVRO, interferometric visibility errors as a result of phasing the array were estimated to be at the 10% level. Data were recorded with the Mk III system (Rogers et al. 1983) and used 14 4 MHz base-band channels, centered near the SiO line: $\nu_{\text{rest}} = 86243.442$ MHz (Lovas 1992). The spectral features of VX Sgr span a range of slightly less than 8 MHz (28 km s^{-1}), but our observations were not optimized to center the SiO line and so the maser signal extends over three of the 14 base-band channels. Correlation was performed at Haystack Observatory using 112 lags in each of these three channels, resulting in a spectral resolution of 0.25 km s^{-1} .

2.2. Calibration and Imaging

Of major concern in all 86 GHz–VLBI experiments is the interferometric phase noise introduced by atmospheric path length fluctuations. This noise limits the time over which the complex visibility can be coherently averaged, and adversely affects array sensitivity. To ascertain the severity of this problem, we averaged the NRAO 530 data by using a range of averaging intervals. Each 3 minute scan was segmented in time, and the amplitudes of coherent averages within each segment were then averaged to estimate visibility amplitude for the entire scan (see Rogers, Doeleman, & Moran 1995). Figure 1 shows the best estimate of visibility amplitude and signal-to-noise ratio (SNR) as a function of segmentation time on each baseline for one representative scan. The coherent integration time corresponding to a 5% amplitude loss is generally between 15 and 30 s. For the data analysis presented here, coherent integrations of 30 s were used throughout, and the absolute flux calibration scale was adjusted upward by 10%. This approach maximized the SNR for fringe-fitting purposes, while limiting calibration problems related to poor coherence to negligible levels.

To perform the amplitude calibration we used the observations of NRAO 530 conducted during the experiment. Following Rogers et al. (1994), we segmented VLBI data on this source to the atmospheric coherence time and averaged them to determine optimal estimates of the raw correlation coefficients. To determine the SEFD for each antenna as a function of elevation angle, we fit segmented and averaged cross-correlation amplitudes (ρ) to the functional form

$$\rho_{ij} = \frac{1}{\sqrt{\text{SEFD}_i \text{SEFD}_j}}, \quad (1)$$

where

$$\text{SEFD}_i \propto \exp\left(\frac{\tau_i}{\sin \theta}\right) - c_i, \quad (2)$$

and τ_i is zenith opacity at antenna i , θ is elevation angle, and c is a constant roughly equal to the ratio of atmospheric temperature to a sum of receiver temperature plus atmospheric temperature. The fitted τ_i and c_i account for atmospheric effects as well as antenna losses, such as spillover. Thus, τ_i and c_i may not reflect actual zenith attenuation and temperature ratios as described above. We find that the τ fit to Kitt Peak is very close to zero and that the calibration on

TABLE 1
CHARACTERISTICS OF ANTENNAS IN THE VLBI ARRAY

Antenna	Diameter (m)	Aperture Efficiency	SEFD at 40° (Jy)
Haystack	37	0.13	8000
Kitt Peak	12	0.6	8000
OVRO	4 × 8	0.6	5000

the Kitt Peak–OVRO baseline depends only on the elevation at OVRO. VX Sgr was not detected on either baseline to Haystack, and those data were not calibrated. A fit to the NRAO 530 data gives $\tau_{\text{OVRO}} = 0.41$ and $c_{\text{OVRO}} = 0.05$. This fit is somewhat sensitive to whether or not NRAO 530 is spatially resolved. A preliminary calibration using only system temperatures and published gain curves showed that NRAO 530 could be as large as 85 μs , which would affect calibration of VX Sgr only at the 2% level. Figure 2 shows the SEFD fit assuming both a point-source structure for NRAO 530 and a Gaussian with FWHM of 85 μs . We note that the spectral template method of amplitude calibration was explored in reducing this data set, but later abandoned. In this method, auto spectra from each antenna are fitted to a best-calibrated template spectrum to determine relative gain fluctuations as a function of time. Auto spectra for Kitt Peak and OVRO, however, exhibited ringing near band edges and noise levels that precluded reliable template fits.

Subsequent imaging made use of the phase-referencing technique (Thompson, Moran, & Swenson 1986), which is commonly applied in spectral line VLBI to produce maps with excellent relative astrometry. Since individual SiO maser features are spatially compact and typically span $\sim 1 \text{ km s}^{-1}$ in velocity, the detection threshold is set by the coherence time. If one maser feature can be identified and detected throughout the observations on timescales smaller than this coherence limit, then its phase solutions can be applied to all other velocity channels in the cross power spectrum. In this way, all other maser features become positionally referenced to this bright component. More importantly, the reference solutions account for atmospheric phase fluctuations, which allows data on faint features to be integrated beyond the usual coherence limits. A caveat of this method is that the selected reference feature must be an unresolved point source or its structure must be well known. If neither of these criteria is met, the intrinsic structure phase of the reference channel will contaminate the other channel maps. Here we describe our application of phase referencing to the VX Sgr masers.

The NRAO AIPS software package was used for both the amplitude calibration described above and the fringe-fitting analysis. The delay calibration and an approximate fringe rate calibration were performed by fringe fitting on NRAO 530. This process accurately calibrated the instrumental delay and rate, since the array geometry and the source position are known to high accuracy. Phase differences between the adjacent 4 MHz bandpasses were also calibrated using NRAO 530. These solutions were transferred to VX Sgr. The position of VX Sgr is known to better than 0".15 (Wright et al. 1990), which limits residual rate and delay errors for the maser emission to the level of a few millihertz and a few nanoseconds, respectively. The latter error, which cannot be solved for using spectral line data,

introduces possible phase errors of up to 2° across the velocity width of the line.

The solution for fringe rate on the line data was attempted on the strongest spectral feature apparent in the raw cross power spectra. High SNR solutions were obtained, but inspection of the data with these fringe rates removed revealed that the channels at the line peak contained strong variations in the visibility function with time. A spectral channel or group of channels was sought that displayed visibility amplitudes that were flat with time, indicative of structure dominated by a point source, and a promising candidate was identified spanning two channels on the blue side of the brightest peak of the spectrum. Fringe fitting on this feature also produced robust solutions that were applied to the remaining channels.

The resulting data set was Fourier inverted and deconvolved in order to detect and locate maser features in all spectral channels. The (u, v) coverage from this single-baseline data set yielded a highly elongated beam pattern with a maximum sidelobe level of 59%. Because of this, the CLEAN algorithm was applied conservatively, employing only 20 iterations at a loop gain of 0.1. A data cube was constructed containing images 0".1024 on a side, and covering the entire velocity width of the line (roughly from -5 to $+25 \text{ km s}^{-1} V_{\text{LSR}}$). Figure 3 shows the beam characteristics and an all-channel map of the maser emission generated by plotting the maximum intensity found over all velocities at each pixel.

The fidelity of the images depends crucially on the degree to which the structure in the reference channels is dominated by an unresolved point source. The transfer of a nonzero structural phase from the reference channel to target channels will in general cause a mirror image of the structure in the reference channel to appear in the referenced image. In addition, since the visibility amplitudes will not reflect such structure, strong sidelobes characteristic of severe amplitude miscalibration will appear, and will be apparent on the images. The structures observed on the channel maps were usually pointlike, with no strong sidelobe patterns evident, which constitutes evidence of pointlike structure and zero phase in the reference channel. The easily discernible maser spots in Figure 3d are good examples.

The structure at the line peak was found to be a double separated by 2.7 mas, confirmed by strong beating evident in the visibility amplitudes. To demonstrate the effects of nonpointlike structure in the reference channel, we phase-referenced the data set to the line peak then imaged other channels. The resulting images reflected the double structure in the reference channel, with power spread across the image as anticipated from the nonphysical combination of phase and amplitude caused by the referencing. These tests, combined with the constancy of the visibility amplitude in our chosen reference channels, gives us confidence that large departures from zero phase in the reference channels, and consequent large phase errors in the phase-referenced data set, are not present. The primary effect of small phase errors will be a contribution to the error budget of the relative position measurements discussed below.

2.3. Image Analysis

The elongated beam shape and sidelobe levels cause the images to be dynamic-range limited. This limit is worse in the presence of complex structure, so that in practice chan-

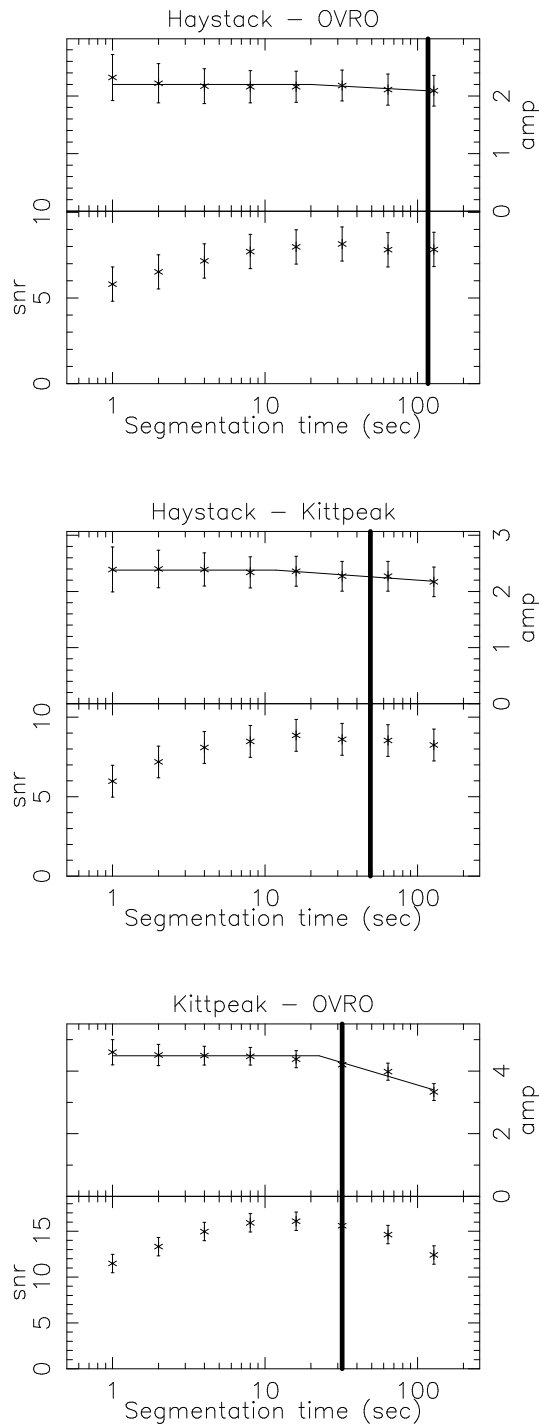


FIG. 1.—Formal fit of baseline-based coherence times to all three baselines among Haystack–OVRO–Kitt Peak using data from the compact radio source NRAO 530. Three minute VLBI scans were segmented at different intervals and scalar averaged to determine visibility amplitude. The amplitude (*upper panels*) for each baseline is fitted in a log-linear plot with a plateau below the coherence time and a linear slope for segmentation times beyond the coherence time. Lower panels for each baseline show the SNR, which peaks at an optimal coherence time that balances coherence losses for long segments with increased noise for very short segments. Good weather at all sites is evident in these plots, which show coherence times of greater than 20 s for all baselines. Thick solid lines mark the segmentation times at which coherence losses are 5%.

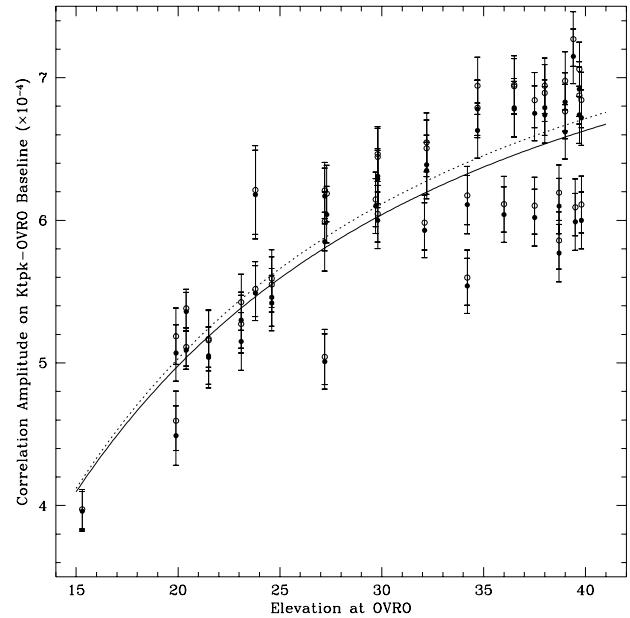
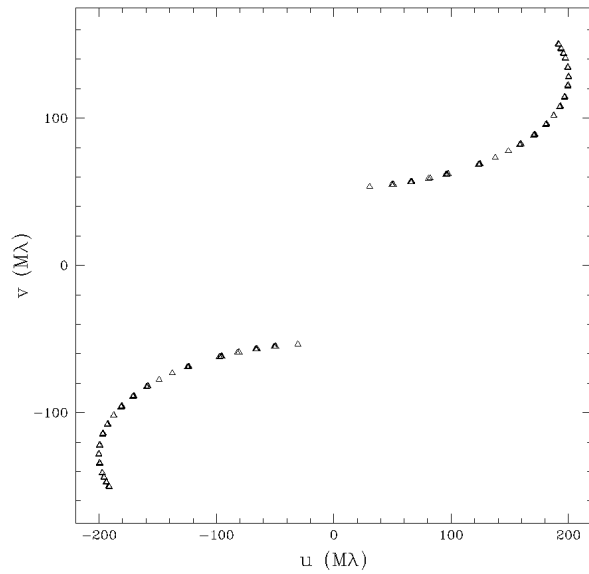
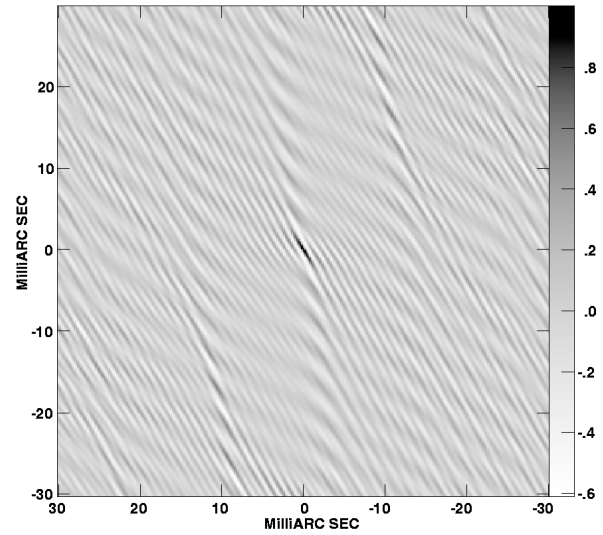


FIG. 2.—Fit of coherence-corrected cross-correlation coefficients on NRAO 530 to eq. (1). Two fits were attempted, one to the data assuming NRAO 530 to be a point source (*filled circles and solid line*) and the other with the correlations adjusted assuming NRAO 530 to be slightly extended with a FWHM of $85 \mu\text{s}$ (*open circles and dotted line*). The size of NRAO 530 was determined by calibrating the long Haystack baselines with system temperatures and gain curve for Haystack.

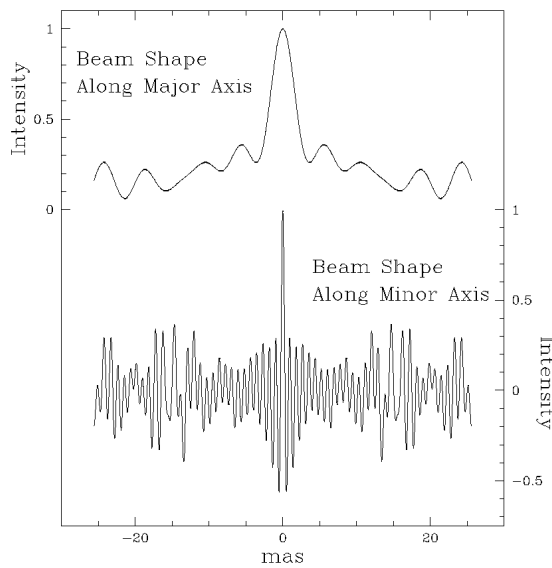
nels with multiple maser components have a higher detection threshold than channels with a single maser spot. The background in the images is strongly non-Gaussian, so a simple SNR criterion for detection is inadequate, and it was necessary to employ a measure of component reliability based on a variety of considerations. These included the contrast of a feature with its surroundings, feature persistence at a precise position across multiple channels, evidence of bad data based on patterns in the map background, and the confusion level caused by sidelobes from multiple features. Maser spot candidates were rejected if, according to these criteria, their physical reality was significantly in question.

Each maser spot was fitted to an elliptical Gaussian brightness distribution to extract position and flux density. Because of conservatism in application of the above criteria, the resulting list is expected to be seriously incomplete at the lower flux density levels, and partially incomplete even at the 7 Jy level. Because of the poor beam shape and lack of (u, v) coverage, combined with the uncertainties described above in phase calibration, no attempt was made to analyze the structure of individual spots, which were treated as point sources. Similarly, due to varying detection thresholds from channel to channel, no attempt was made to fit line velocity profiles for the maser components, beyond noting line widths generally of order 0.5 km s^{-1} . The maser spot flux densities and locations, plotted for each separate channel, are displayed in Figure 4.

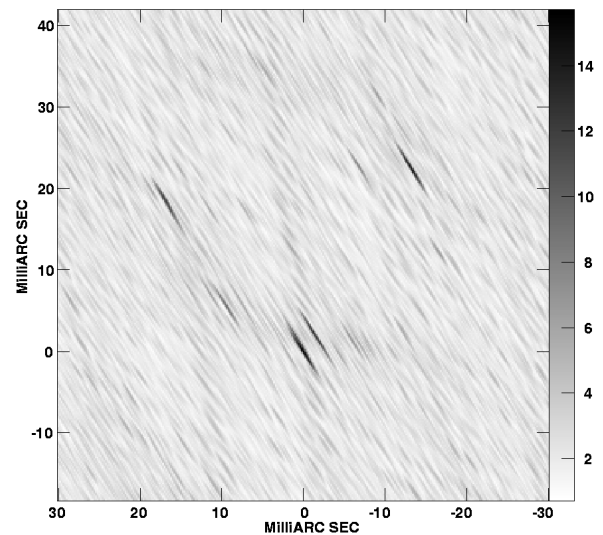
The relative positions of maser spots have uncertainties related to the phase errors present in the referenced data set. These phase errors arise from multiple sources. First, thermal phase noise introduces uncertainties, but in all cases such errors are insignificant. Much larger phase errors are possible because of imperfect delay calibration, which introduces a spurious phase slope with frequency. In our

(a) (u, v) coverage

(b) Interferometric beam



(c) Beam shape



(d) All channel map

FIG. 3.—Figures illustrating the interferometric beam and a resulting channel map. (a) (u, v) coverage of both observing days combined. (b) “Dirty beam” formed by Fourier inverting the (u, v) coverage. (c) Slices through the major and minor axes of the beam in (b) showing the well-defined minor axis beam and its maximum sidelobe of 60%. (d) All-channel map showing the maximum intensity at each pixel over a velocity range of -7.1 to 25.9 km s^{-1} . The Gaussian restoring beam is $5.8 \times 0.4 \text{ mas}$ FWHM at P.A. of 32° .

case, with accurate absolute astrometry available for the star, the delay-related phase error should not exceed 2° . Another source of phase error is nonzero structural phases in the reference channels, transferred to the rest of the data set in the phase-referencing operation. Based on the tests described above for major departures from pointlike structure in the reference channel, we estimate that any additional features in the reference channel do not total more than 30% of the flux density of the main pointlike feature. This translates to potential phase errors throughout the data set on the order of 20° . Other sources of phase error are negligible, and this translates to a 3σ positional uncer-

tainty of about 0.2 beamwidths for all components, which is shown in Figure 4.

The total maser spectrum, derived from autocorrelation data at OVRO, together with the VLBI-scale source spectrum derived as described below, are shown in Figure 5. In general, we detect $\sim 20\%$ of the total flux density on the Kitt Peak–OVRO baseline with visibilities rising to 0.65 near $v = 19 \text{ km s}^{-1}$. This finding is in general agreement with the 43 GHz result of Greenhill et al. (1995) and provides clear evidence for coherent masing structure on scales larger than 0.4 mas (0.7 AU). Since the maser spot list is incomplete, the cross power spectrum was not formed from

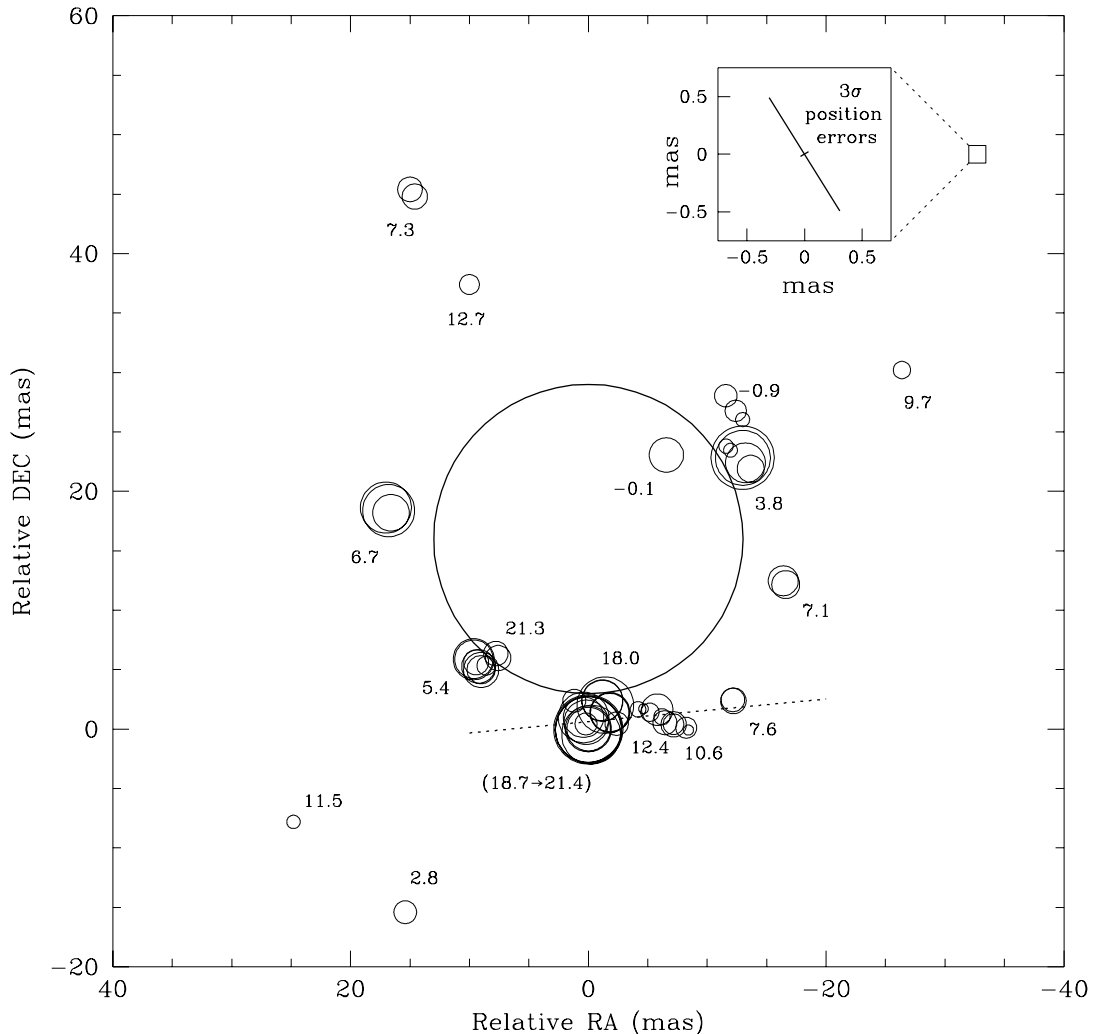


FIG. 4.—Location and flux density of the brightest 86 GHz maser spots. Each distinct feature is represented by a circle whose radius is proportional to flux density. Flux density ranges from 2 Jy for the weakest component to 14.6 Jy for the phase reference feature that sits at the map (0, 0) point. Also shown is the disk of VX Sgr with an assumed diameter of 26 mas and a presumed location roughly concentric with the shell of masers. The dotted line threading the southern complex of maser features shows the direction in which we find a linear velocity gradient. Individual maser spots are labeled with LSR velocities in km s^{-1} , and groups of masers are labeled with average velocities where appropriate. In the upper right-hand corner, an inset shows the 3σ positional errors. Dotted lines connect the inset to a scaled square that emphasizes the relative scales in the error plot.

a sum of flux density from each cross-correlation channel map. Instead, we averaged the data set to an interval of 180 s and searched in time for a maximum correlated flux density in each velocity channel. The positive bias introduced by the maximum search was removed by requiring zero-correlated flux density beyond the overall line extent. To account for coherence losses incurred by averaging to the full scan length of 180 s, the resulting maximum cross power spectrum was increased by a factor of 1.2. Noise in individual channels near the edge of the spectrum had a measured 3σ of 5 Jy.

3. DISCUSSION

3.1. Maser Emission Structure

Recent work has clearly shown that 43 GHz SiO maser features form rings of emission tracing long tangential gain paths around the stellar disk (Diamond et al. 1994; Greenhill et al. 1995; Humphreys et al. 1996; Kemball & Diamond 1997; Diamond, Kemball, & Boboltz 1997). The 86 GHz emission in Figure 4 appears similarly arranged

with a maximum component separation of 40 mas and a ring diameter of 30 mas. Direct photospheric radius measurements of VX Sgr are difficult to obtain given its low Galactic latitude. Greenhill et al. (1995) use IR interferometry at $11\ \mu\text{m}$ to model the encircling dust shell and assume a model of radiative transfer to arrive at a stellar radius of 13 mas (22 AU). The large central circle in Figure 4 shows the scale of such a stellar disk, although an exact registration of the star with the maser emission is not possible. If this radius for VX Sgr is valid, then the maser ring in this star forms much closer ($r < 1.5r_*$) than 43 GHz masers found in the envelope of TX Cam and U Her ($r \sim 2r_* - 4r_*$; Diamond et al. 1994). A time separation of nearly two years precludes a direct comparison of our results with the 43 GHz maser image of VX Sgr by Greenhill et al. (1995). In general, though, masers at both frequencies are found at nearly the same radius and both suggest a ring structure, placing masers from the two transitions in the same circumstellar region and general environment.

A surprising feature of the 86 GHz emission is an apparent velocity gradient along a group of southern maser spots

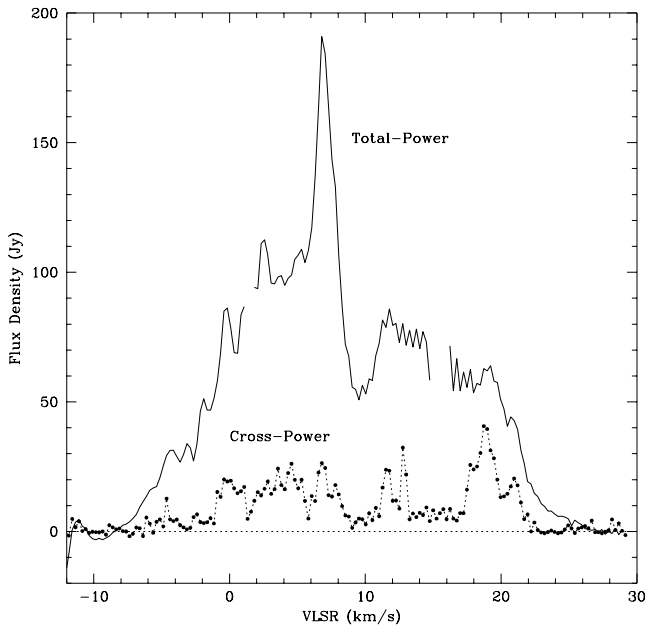


FIG. 5.—Comparison of total power auto spectra from the OVRO phased array with the cross power spectrum on the OVRO–Kitt Peak baseline. The solid line shows the total power spectrum that has small gaps near the band edges of the three 4 MHz base-band converters used in the Mk III system. The cross power spectrum was formed by taking the maximum at each velocity channel over the 2 days of observation as computed using a full VLBI scan of 180 s. Each channel was then noise debiased, and corrected for both bandpass effects and a 20% coherence loss. The maximum visibility of 0.65 occurs near $V_{\text{LSR}} = 19 \text{ km s}^{-1}$, and near the 185 Jy peak the visibility is only 0.14. Based on these data, most of the maser emission must occur on scales larger than our 0.4 mas beam.

near the reference component. This gradient appears in the strongest complex of maser spots in the source, which is aligned roughly east-west on the southern edge of the ring. Fortunately, this extension is roughly perpendicular to the major axis of our highly elongated beam, allowing us to achieve fine spatial resolution across the complex. To characterize this gradient, a linear relation was first fitted to the locations of the southern maser components. Points in the (α, δ) sky plane were rotated to the beam major axis at P.A. = 32° so that exact 1σ positional errors along the beam axes could be used. A χ^2 minimization found the best-fit line to have a P.A. of 95° east of north as shown by the dotted line in Figure 4. A second fit of maser velocity as a function of projected distance along this fitted positional axis yields a velocity gradient of $-1.04 \text{ km s}^{-1} \text{ mas}^{-1}$. Figure 6 shows this gradient with data for each separate maser feature in each velocity channel. It is certain that some measured maser components in adjacent velocity channels are part of the same physical maser component that is resolved in velocity. The incompleteness of our maser spot list prohibits a meaningful fit to the velocity profiles of these physical maser components. This makes a formal error estimate for the velocity gradient difficult because the errors on the velocity axis are poorly determined. A conservative visual inspection shows that uncertainty in the derived gradient is probably 20%.

Maser velocity structure is a tracer of stellar envelope kinematics and can help disentangle the effects of rigid stellar rotation from mass-loss outflows. Such gradients are often sought as clues to envelope dynamics, but most of the 43 GHz VLBI work done so far has been unable to produce

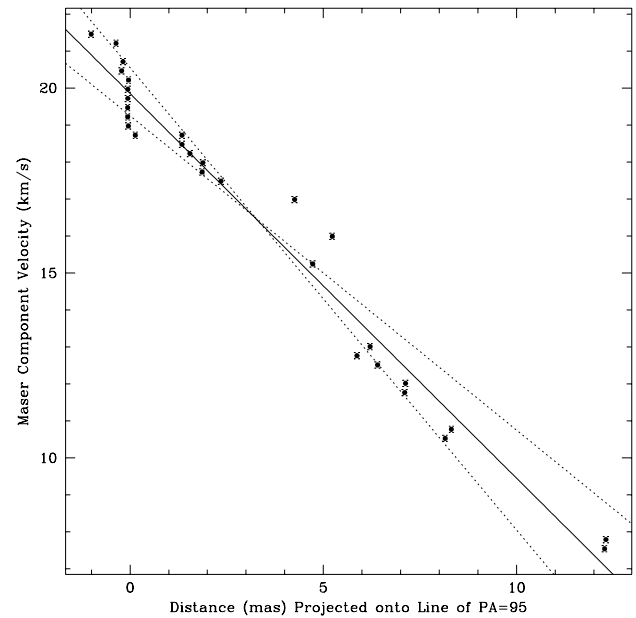


FIG. 6.—Least-squares fit to the velocity gradient seen among the southern complex of maser features. In this plot, maser spots in different velocity channels are considered as individual maser features, but it is likely (see text) that spots seen at the same position in multiple channels are physically related. This complicates any estimate of velocity gradient error. The solid line shows the best-fit linear velocity gradient. The two dotted lines show slopes of $\pm 20\%$ of the best-fit value for comparison.

convincing examples. Diamond et al. (1994) show a slight velocity gradient across the 26 mas diameter of TX Cam, but the drift is hardly monotonic and amounts to only $0.36 \text{ km s}^{-1} \text{ AU}^{-1}$ at a distance of $\sim 317 \text{ pc}$ (Patel, Joseph, & Ganesan 1992). They are able to model this velocity slope as either a rotation of the stellar envelope or by orientation effects alone. By comparison, the velocity gradient observed in VX Sgr at 86 GHz maintains a nearly constant $0.6 \text{ km s}^{-1} \text{ AU}^{-1}$ over a spectral span of 13 km s^{-1} , extending to nearly 22 AU in the east-west direction. More recent work by Diamond (1997, private communication) shows that the velocity structure in TX Cam is more complicated than a simple gradient. Instead, as one traces the maser ring, the velocities steadily increase from the most blueshifted components all the way around the star, so that the most redshifted masers are found near the most blueshifted ones. It is clear that this is not the case for VX Sgr. In Figure 4 the lowest velocities are found in a group of masers in the upper right, while the highest velocity features are located on the other side of the star near the map (0, 0) point. Such a distribution of extreme velocities is suggestive of stellar rotation, though the overall velocity field is clearly complex.

Although detailed dynamic modeling is not possible using this data set, we can investigate the plausibility of various models for the velocity gradient. Linear velocity gradients are characteristic of solid-body rotation, so it is natural to question whether the masers could be coupled to the rotation of the star itself. Such coupling is plausible on the grounds that evidence exists for dynamically important magnetic fields permeating the maser regions (Barvainis, McIntosh, & Predmore 1987; Kembell & Diamond 1997), which could corotate with the star. The 13 km s^{-1} range of velocities in the southern group of features does not evenly bracket the systemic stellar velocity, which we take to be 5.3 km s^{-1} (Chapman & Cohen 1986). The fact that the entire

complex is redshifted implies that the pole of rotation would have to be close to position angle 45° east of north. The angular extent of the complex is ~ 13 mas, or about 1 stellar radius, which implies a minimum photospheric equatorial velocity of $\sim 13(\sin i)^{-1} \text{ km s}^{-1}$ if the axis of rotation is inclined i degrees to our line of sight. This maximum velocity exceeds estimates of the photospheric velocity of $\pm 10 \text{ km s}^{-1}$ derived from optical spectroscopy (Wallerstein & Fawley 1980), but it is unclear whether the existence of such velocities near the stellar limb at the equator is ruled out by such observations. The normal interpretation of such velocity widths in optical data is, however, in terms of radial motion, and it remains to be seen whether a rotational interpretation is plausible. The observed velocity gradient is of the same approximate magnitude as the optical velocities, raising the possibility of a direct connection.

Accurate determination of rotational velocities of evolved stars is challenging owing to their complex molecular spectra in which many lines are confusingly blended. In addition, the signature form of line broadening indicating rotation can be hidden by other broadening phenomena such as macroturbulence and optical depth variations (Barnbaum, Morris, & Kahane 1995). Recent near-IR work on the evolved carbon star V Hya (Barnbaum et al. 1995) estimates that the star's pulsations are accompanied by variations in rotational velocity of 9 km s^{-1} . The authors set a maximum absolute rotational velocity of $\sim 18 \text{ km s}^{-1}$. Barnbaum et al. (1995) note, though, that such a large velocity for a giant star is rare and cannot be achieved without postulating a common envelope binary scenario.

It is clear from all recent SiO maser VLBI experiments that the inner envelope of evolved stars is a highly inhomogeneous environment. Our nondetections on long 86 GHz baselines place a lower limit of ~ 0.1 mas on strong maser spot sizes, which agrees with the angular sizes of the strongest features seen at 43 GHz in VX Sgr (Greenhill et al. 1995). This would also seem to be a lower limit to the size scales of strong inhomogeneities in the circumstellar medium. Hitherto, a plausible upper limit to these size scales has been the sizes of maser complexes at similar velocities seen in 43 GHz images. Our detection of an apparently coherent structure 13 mas long with a systematic velocity gradient constitutes evidence, however, of clumpiness in the medium on size scales comparable to the stellar radius. Any model that seeks to explain the properties of these stars and their circumstellar environments, such as those involving turbulence (Hartquist & Dyson 1997), must predict structure on these large scales.

3.2. Pump Mechanisms

Consensus among proponents of rival pumping mechanisms remains distant, and both radiative and collisional excitation models require verification by high-resolution comparisons of different maser transitions. This is illustrated by the results of Miyoshi et al. (1994), which showed cospatial $v = 1$ and $v = 2$ masers in the $J = 1 \rightarrow 0$ rotational transition, and allowed a strong argument in favor of collisional pumping.

In the case of comparison between $v = 1, J = 1 \rightarrow 0$ and $J = 2 \rightarrow 1$ masers, the evidence for cospatiality relies heavily on the similarities of single-dish line profiles and polarization characteristics (McIntosh & Predmore 1993). The results of Colomer et al. (1996) using 86 GHz connected element interferometry are likewise suggestive but inconclu-

sive regarding registration between these two maser transitions. Competing theories appear to agree that, for the most part, rotational transitions in the same vibrational state should be found in the same physical conditions. Doel et al. (1994) use a model of SiO emission that includes effects of dust emission, stellar radiation, and collisions to show that both $v = 1, J = 1 \rightarrow 0$ and $J = 2 \rightarrow 1$ masers can coexist in the same region via *either* collisional or radiative excitation. Rausch et al. (1996) develop a model taking into account line emission from the stellar photosphere that supports a radiatively pumped scheme also allowing cospatial $v = 1, J = 1 \rightarrow 0$ and $J = 2 \rightarrow 1$ masers.

The results presented here demonstrate the feasibility of future 43 and 86 GHz SiO maser comparisons and the accuracy they might attain. The newly formed Coordinated Millimeter VLBI Array² (CMVA), under whose auspices these data were reduced, can provide up to 11 antennas for 86 GHz spectral line VLBI. The formal position errors for the maser components shown in Figure 4 can be greatly reduced by observing with a number of antenna sufficient to allow self-calibration of structure in the phase reference channel. With better (u, v) coverage, somewhat longer baselines, and SNR values on the stronger maser features of several tens, relative positional accuracies between features of a single transition approaching 10 mas are possible. By cross-correlating the structures seen between transitions, positional registration at a level a few times this is possible. This accuracy represents scales which are small compared to the maser spot sizes, so that, as opposed to merely setting limits on positional offsets, a definitive statement on cospatiality, or the absence thereof, can be made.

4. CONCLUSIONS

We have shown that the SiO maser emission in the $v = 1, J = 2 \rightarrow 1$ 86 GHz transition has a spatial structure similar to that found at 43 GHz, both in this source and in others of its class. Given the physics of these systems, with a fairly narrow shell of potentially favorable conditions for the existence and pumping of SiO in the gaseous phase around the star, it would have been remarkable for the 86 GHz masers to have arisen elsewhere. This work has produced two results of note. First, we have achieved precision relative astrometry for the 86 GHz masers, which opens the way to precise relative astrometry between SiO maser transitions, a development that will provide new constraints on models of these masers. Second, we have discovered a strong, monotonic, large-scale linear velocity gradient that is adequately modeled by solid-body rotation, a feature hitherto unknown in these sources. The gradient could arise either as a result of true rotation, possibly associated with the rotation of the star, or from systematic motions in the stellar atmosphere, presumably associated with the mass loss, on larger scales than were previously known to exist. Further progress regarding both these results must await more comprehensive observations.

² Support for the Coordinated Millimeter VLBI Array work at the Haystack Observatory is provided under a grant from the NSF to the Northeast Radio Observatory Corporation.

REFERENCES

- Alter, G., Balázs, B., & Ruprecht, J. 1970, *Catalogue of Star Clusters and Associations* (2d ed.: Budapest: Akad. Kiadó), 2379
- Barnbaum, C., Morris, M., & Kahane, C. 1995, *ApJ*, 450, 862
- Barvainis, R. E., McIntosh, G. C., & Predmore, C. R. 1987, *Nature*, 329, 613
- Barvainis, R. E., & Predmore, C. R. 1985, *ApJ*, 288, 694
- Bujarrabal, V. 1994a, *A&A*, 285, 953
- . 1994b, *A&A*, 285, 971
- Celis, L. 1995, *ApJS*, 98, 701
- Chapman, J. M., & Cohen, R. J. 1986, *MNRAS*, 220, 513
- Colomer, F., Baudry, A., Graham, D. A., Booth, R. S., De Vicente, P., Krichbaum, T. P., Gomez-Gonzalez, J., & Schalinski, C. 1996, *A&A*, 312, 950
- Diamond, P. J., Kembell, A. J., & Boboltz, D. A. 1997, *Vistas Astron.*, 41(2), 175
- Diamond, P. J., Kembell, A. J., Junor, W., Zensus, A., Benson, J., & Dhawan, V. 1994, *ApJ*, 430, L61
- Doel, R. C., Gray, M. D., Humphreys, E. M. L., Braithwaite, M. F., & Field, D. 1995, *A&A*, 302, 797
- Elitzur, M. 1992, *ARA&A*, 30, 75
- . 1996, *ApJ*, 457, 415
- Greenhill, L. J., Colomer, F., Moran, J. M., Backer, D. C., Danchi, W. C., & Bester, M. 1995, *ApJ*, 449, 365
- Hartquist, T., & Dyson, J. 1997, *A&A*, 319, 589
- Humphreys, E. M. L., Gray, M. D., Yates, J. A., Field, D., Bowen, G., & Diamond, P. J. 1996, *MNRAS*, 282, 1359
- Kembell, A. J., & Diamond, P. J. 1997, *ApJ*, 481, L111
- Kholopov, P. N., et al. 1987, *General Catalogue of Variable Stars* (4th ed.; Moscow: Nauka)
- Knapp, G. R., & Morris, M. 1985, *ApJ*, 292, 640
- Lockett, P., & Elitzur, M. 1992, *ApJ*, 399, 704
- Lovas, F. J. 1992, *J. Phys. Chem. Ref. Data*, 21, 181
- McIntosh, G. C., & Predmore, C. R. 1993, *ApJ*, 404, L71
- McIntosh, G. C., Predmore, C. R., & Patel, N. A. 1994, *ApJ*, 428, L29
- Miyoshi, M., Matsumoto, K., Kamenoi, S., Takaba, H., & Iwata, T. 1994, *Nature*, 371, 395
- Nedoluha, G. E., & Watson, W. D. 1994, *ApJ*, 423, 394
- Patel, N. A., Joseph, A., & Ganesan, R. 1992, *J. Astrophys. Astron.*, 13, 241
- Pijpers, F. P., Pardo, J. R., & Bujarrabal, V. 1994, *A&A*, 286, 501
- Rausch, E., Kegel, W. H., Tsuji, T., & Piehler, G. 1996, *A&A*, 315, 533
- Rogers, A. E. E., et al. 1983, *Science*, 219, 51
- . 1994, *ApJ*, 434, L59
- Rogers, A. E. E., Doeleman, S., & Moran, J. 1995, *AJ*, 109, 1391
- Thompson, A., Moran, J., & Swenson, G. 1986, *Interferometry and Synthesis in Radio Astronomy* (New York: Wiley)
- Wallerstein, G., & Fawley, W. M. 1980, *PASP*, 92, 183
- Wright, M. C. H., Carlstrom, J. E., Plambeck, R. L., & Welch, W. J. 1990, *AJ*, 99, 1299